PHYSICAL REVIEW A VOLUME 57, NUMBER 1 JANUARY 1998

Final ion-charge resolving electron spectroscopy for the investigation of atomic photoionization processes: Xe in the region of the $4d \rightarrow \epsilon f$ resonance

T. Luhmann, Ch. Gerth, M. Groen, M. Martins, B. Obst, M. Richter, and P. Zimmermann
Institut für Atomare und Analytische Physik, Technische Universität Berlin Hardenbergstrasse 36, 10623 Berlin, Germany

(Received 12 August 1997)

Electron-ion coincidence spectroscopy of energy-analyzed electrons and charge-separated ions is used to investigate complex decay processes of atoms after inner-shell photoionization with monochromatized synchrotron radiation. Improvements in the experimental technique allow a complete electron spectrum resolved into the different contributions of the final ion-charge states to be measured. This method of final ion-charge resolving electron spectroscopy is demonstrated by the example of xenon for different photoionization processes in the region of the $4d \rightarrow \epsilon f$ resonance. [S1050-2947(98)04401-1]

PACS number(s): 32.80.Fb, 32.80.Hd

I. INTRODUCTION

Photoionization studies of complex decay processes of atoms after inner-shell excitation usually take advantage of the detailed information obtained from photoelectron spectra. For a deeper insight into the different decay routes, however, the results of photoelectron spectra may be combined with those of photoion spectra, which give the different charge states of the photoions as final products of the decay processes. The best combination of both is realized by the technique of photoelectron-photoion coincidence spectroscopy, whereby one can relate an initial ionic state designated by the photoelectron signal to the final charge state of the photoion after deexcitation by fluorescence or Auger decay.

Photoelectron-photoion coincidence spectroscopy has often been applied to study threshold electrons in noble gases [1–5]. This approach has the advantage of a high angular acceptance for ''zero volt'' electrons. Photoelectron-photoion coincidence studies with energy-resolved photoelectrons were presented by Shigemasa *et al.* [6] in the $3d$ region of Kr, by Kämmerling *et al.* [7] in the $4d$ region of Xe, and by Baier *et al.* [8] in the $4d$ region of Ba. A further development of the method was achieved by Luhmann *et al.* [9] who succeeded in recording a complete electron spectrum resolved into the different contributions of the final ion-charge states. For this kind of electron spectroscopy the abbreviation FIRE (final ion-charge resolving electron) spectroscopy was proposed.

Due to the different angular acceptance of energy-analyzed electrons and charge-separated ions, the main problem for such a coincidence experiment is the distinction between ''true'' and ''false'' coincidences. The demand for a low number of false coincidences thereby is in contrast with the need for a short data accumulation time. This difficulty of the coincidence measurements is even more pronounced when satellite processes are investigated, which have a low cross section in comparison with the main photoionization processes. In these cases the main processes due to their different ionization energies are separable in the electron ''branch'' but still act as ''background'' processes in the ion ''branch'' and drastically increase the number of false coincidences. The experimental setup and method will be discussed in this paper, the evaluation procedure to solve the problem of false coincidences is discussed in detail in Ref. [10]. The power of the method will be demonstrated by photoionization of Xe in the region of the $4d \rightarrow \epsilon f$ resonance.

II. EXPERIMENT

In our experiments we have investigated the photoionization of free atoms by energy-analyzed photoelectron-photoion coincidence spectroscopy. A correlated analysis of electron-ion pairs is performed by combining photoelectron and photoion spectroscopy. In coincidence measurements it is essential (a) that both spectrometers have a common geometrical acceptance area, and (b) that the time correlation of coincident electron and ion signals is preserved by the electronics.

A. Basic setup

Figure 1 illustrates the experimental setup and its most important components. A continuous beam of free atoms, which is produced either by a gas nozzle (gaseous samples) or by an atomic beam source (solid or liquid samples), crosses a beam of monochromatized synchrotron radiation (SR). In the present experiments on Xe the SR was provided by the toroidal grating monochromator TGM4 at the electron storage ring BESSY in Berlin (Germany). Photoemitted electrons are analyzed for their kinetic energy ϵ by a cylindrical mirror analyzer (CMA), corresponding ions are separated by their mass to charge ratio m/q using a Wiley-McLaren type time-of-flight spectrometer (TOF) [11]. In both analyzers, particle detection is performed by two-stage microchannel plates (MCP).

To account for the angular distribution of photoelectrons, the CMA only accepts electrons with an angle of emission close to the ''magic'' angle ($54.7° \pm 1.7°$ with respect to the spectrometer axis), thereby integrating an azimuth of 180°. This results in an accepted solid angle of 1.22% of 4π with respect to a point source centered in the interaction region. In comparison with a ''full'' 360° CMA, whose accepted solid angle is twice as large, the atomic beam source can, with a 180° CMA, be located much closer to the spectrometer axis

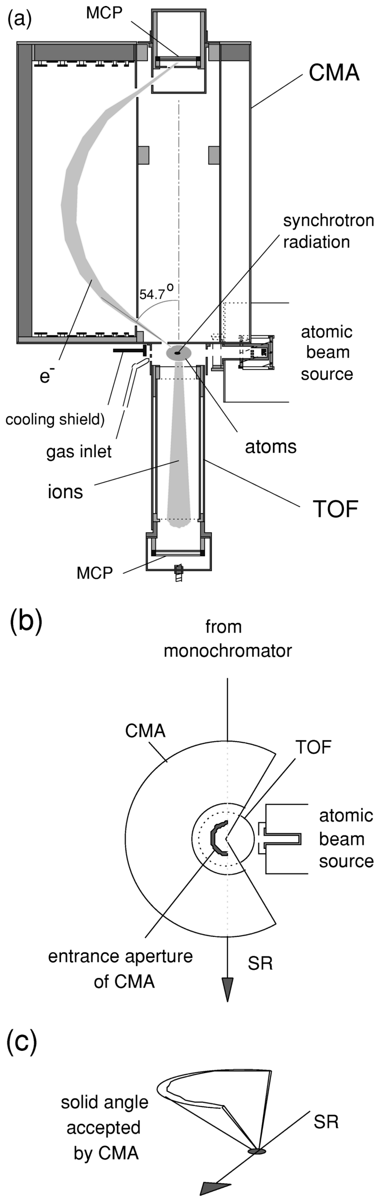

FIG. 1. (a) View from the side of the experimental setup showing cylindrical mirror electron analyzer (CMA), time-of-flight ion analyzer (TOF), and gas inlet. The synchrotron radiation beam is directed towards the observer. (b) View from above (SR is synchrotron radiation). (c) Shape of solid angle accepted by CMA. Atomic beam source and cooling shield are used for experiments on metal atoms (for example, see Ref. [9]).

[Fig. 1(b)], yielding a beam density up to ten times higher in the interaction region. The accepted solid angle has the lateral surface of a half cone, as shown in Fig. 1(c). The CMA has a measured energy resolution $\Delta E/E$ of 1.00(7)%.

While electrons with an appropriate angle of emission reach the CMA due to their kinetic energy, thermal photoions are accelerated towards the TOF by an electrical extraction pulse (-40 V, 4 μs), which is applied to the entrance aperture of the TOF. The front plate of the CMA acts as the opposite electrode (ground level). Having passed the entrance aperture (∅ 6 mm), the ions are postaccelerated in a second acceleration stage of about -60 V before reaching the field-free 116-mm drift region and finally being accelerated onto the detector by an acceleration voltage U_{acc} of

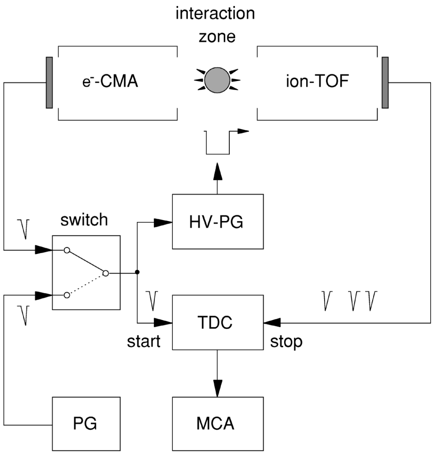

FIG. 2. Principal electronic setup used for electron-ion coincidence measurements and for ‘‘standard’’ TOF measurements (PG is the pulse generator, MCA is the multichannel analyzer, HV-PG is the high voltage pulse generator, TDC is the time-to-digital converter).

-2.5 to -3 kV. Deviating from the original Wiley-McLaren technique, in our TOF the second acceleration stage is not held at a constant voltage, but it is pulsed synchronously with the extraction pulse, and between the pulses all voltages (except the detector) are held at ground level. By this change in the technique the background ion signal in the TOF spectra was drastically reduced. With the second stage held at a constant negative voltage, as in the original setup, a large number of randomly produced ions enter the TOF spectrometer, which give rise to uncorrelated detector signals.

In the setup the axial distance between the CMA front plate and the interaction region is fixed at 8 mm while the respective distance between the interaction region and TOF entrance aperture is variable between 2 and 16 mm by moving the whole TOF inwards and outwards. This facilitates fine adjustments without breaking the vacuum. The three field-limiting meshes of the TOF have an open area of 87% each. This corresponds to a total axial transmission of $\geqslant 66\%$.

B. Coincidence measurements

Time correlation between electron and ion signals is measured by a coincidence circuit shown in Fig. 2. The method takes advantage of the fact that the investigated electrons ($15\ \mathrm{eV} \leqslant \epsilon \leqslant 100\ \mathrm{eV}$) move much faster than the thermal photoions. Thus, an electron signal is available when the corresponding photoion is still located very close to the position where the ionization process took place. A coincidence measurement is performed by using signals of the electron detector for (a) triggering the ion extraction pulse and (b) starting an ion TOF measurement on a time-to-digital converter (TDC). Analyzed photoions that produce coincidence signals at the detector are registered in the stop input of the TDC.

If the analyzer energy of the CMA is fixed during the measurement, a TOF *coincidence spectrum* of photoions correlated with electrons of a specific kinetic energy ϵ is obtained. Characterizing the different ion species by their analyzed final charge state n, $p(\epsilon,n+)$ denotes the probability for the correlation of n-fold charged photoions to electrons of the selected kinetic energy ϵ. For each ϵ, these probabilities are the *measured quantities* of the coincidence experiment and a normalization relation

$$\sum_{n+} p(\epsilon,n+)=1 \tag{1}$$

holds, if the index n runs over all occurring final charge states. It is an advantage of the ion TOF method that for a specific ϵ the correlation probabilities $p(\epsilon,n+)$ of all final charge states $n+=1+,2+,\ldots$ are measured simultaneously. How useful this information is in the analysis of photoionization processes is described in Sec. III.

Due to a number of distorting effects, however, the relative intensities of the different ion species in a coincidence spectrum do not represent the probabilities $p(\epsilon,n+)$ directly. The main effects are (a) the occurrence of false starts and false coincidences, (b) the finite transmission $\tau(n+)$ of the TOF spectrometer, (c) the detection efficiency $\eta(n+)$ of the ion detector, and (d) the dead time in the coincidence signal registration. Depending on the experimental conditions, the effects may be very strong, and additional experimental and analytical efforts are necessary to extract the desired probabilities $p(\epsilon,n+)$.

In the following, the origin of the different distortions will be described and the method of extraction of the probabilities $p(\epsilon,n+)$ from the measured data will be explained.

True and false coincidences

Signals from the electron ''branch,'' which initiate a TOF measurement, are denoted as *starts*. Registrable signals from the ion detector, which arrive at the TDC stop input, are denoted as *coincidences*. In the coincidence experiment specific electron-ion pairs are selected due to their correlation in time. If a certain electron triggers a TOF measurement cycle for the ion belonging to it, a *true* start has occurred, and the ion is called a *true* ion. A *true* coincidence is observed, if the true ion produces a registrable detector signal. Correspondingly, the signals of all other ions are called *false* coincidences. Only false coincidences are observed if the TOF analysis is triggered by a *false* start, e.g., by a dark pulse from the electron detector or by a pulse from a random pulse generator. While a TOF cycle is active, further trigger signals are omitted. It is important to note that due to the correlation of a true start with *one* true ion, *at most one* true coincidence may occur in any TOF cycle. In contrast to this, there is no limit to the number of false coincidences. In a TOF coincidence spectrum, which represents the result of a measurement, true and false coincidences are superimposed, and they are indistinguishable from each other.

For each final charge state $n+$ the average number of false (index F) and true (index T) coincidences per TOF cycle is given by

$$\overline{n_F}(n+)=\overline{N}(n+)\,\tau(n+)\,\eta(n+), \tag{2a}$$

$$\overline{n_T}(n+)=p(\epsilon,n+)p_{\mathrm{TS}}(\epsilon)\,\tau(n+)\,\eta(n+)>1. \tag{2b}$$

Here, $\overline{N}(n+)$ is the average number of false ions analyzed in a TOF cycle. It is connected with the ion production rate $R(n+)$ by a proportionality factor Δt:

$$\overline{N}(n+)=R(n+)\Delta t. \tag{3}$$

$p_{\mathrm{TS}}(\epsilon)$ is the probability of a true start occurring in the measurement:

$$p_{\mathrm{TS}}(\epsilon)=\frac{R_{\mathrm{TS}}(\epsilon)}{R_{\mathrm{TS}}(\epsilon)+R_{\mathrm{FS}}(\epsilon)} \tag{4}$$

(R_{TS} and R_{FS}: rates of true and false starts, respectively).

Considering the ratio of the average numbers from Eqs. (2a) and (2b) [with Eqs. (3) and (4)],

$$\frac{\overline{n_F}(n+)}{\overline{n_T}(n+)}=\frac{1}{p(\epsilon,n+)}R(n+)\Delta t\left(1+\frac{R_{\mathrm{FS}}(\epsilon)}{R_{\mathrm{TS}}(\epsilon)}\right), \tag{5}$$

we find that an experimentally favorable, i.e., small ratio is achieved only if (a) the correlation probability $p(\epsilon,n+)$, that is to be measured, is high, (b) the ion production rate $R(n+)$ is low, and (c) the rate of false starts, $R_{\mathrm{FS}}(\epsilon)$, is small in comparison with the rate of true starts, $R_{\mathrm{TS}}(\epsilon)$. The latter is usually the case when photolines with high intensity are investigated. However if the background in photoelectron spectra is analyzed the rate of true starts may be dramatically low. In these cases, increasing $R_{\mathrm{TS}}(\epsilon)$ by raising up the total rate of ionization events brings about no statistical advantage, because $R(n+)$ is also increased, which compensates the effect. The factor Δt is discussed in Ref. [10].

An expression for $p(\epsilon,n+)$ in terms of measurable quantities is obtained by solving Eq. (2b) for $p(\epsilon,n+)$,

$$p(\epsilon,n+)=\frac{1}{\tau(n+)}\,\frac{1}{\eta(n+)}\,\frac{\overline{n_T}(n+)}{p_{\mathrm{TS}}(\epsilon)}, \tag{6}$$

and then dividing the right side of Eq. (6) by the corresponding sum of all occurring charge states [making use of Eq. (1)]:

$$p(\epsilon,n+)=\frac{[1/\hat{\tau}(n+)][1/\hat{\eta}(n+)]\overline{n_T}(n+)}{\Sigma_{k+}[1/\hat{\tau}(k+)][1/\hat{\eta}(k+)]\overline{n_T}(k+)}. \tag{7}$$

Here,

$$\hat{\tau}(n+)=\frac{\tau(n+)}{\tau(n_0+)} \quad \text{and} \quad \hat{\eta}(n+)=\frac{\eta(n+)}{\eta(n_0+)} \tag{8}$$

are the relative transmissions and detection efficiencies of ions with charge state $n+$ with respect to ions with charge state n_0+ (n_0+ is a fixed charge state, e.g., 1+). These relative quantities can be handled experimentally much more easily than absolute quantities.

Relative ion transmissions

As can be seen from Eq. (7), only the relative transmissions of true ions are relevant for the determination of $p(\epsilon,n+)$. Due to the cylindrical symmetry of the TOF spectrometer we may distinguish between radial and axial transmission. The radial transmission is again split up into a static factor τ_{stat} and a dynamic factor τ_{dyn}:

$$\tau(n+)=\tau_{\mathrm{stat}}\tau_{\mathrm{dyn}}(n+)\,\tau_{\mathrm{axial}}. \tag{9}$$

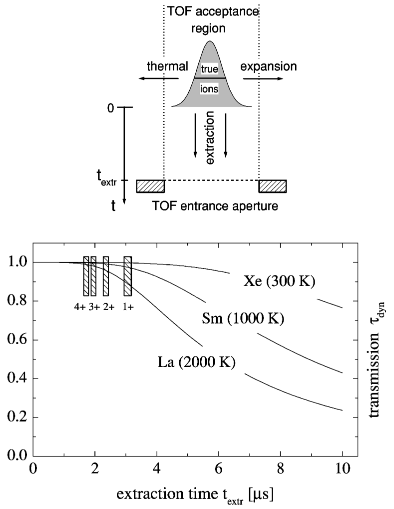

FIG. 3. Upper part: schematic illustration of the dynamic transmission of true ions. Due to their thermal energy, true ions may drift out of the TOF acceptance region during the extraction process and are lost for the analysis. Lower part: result of a model calculation of the dynamic transmission for three elements at different temperatures. Striped vertical bars indicate extraction times of differently charged ions in the experiment.

The factor τ_{stat} takes into account the spatial overlap of the acceptance regions of the two spectrometers, TOF and CMA, with the synchrotron radiation and the atomic beam. By definition, true ions are always produced within the acceptance region of the CMA, since respective electrons must be detected (cf. definition of true ions above). τ_{stat} then denotes the fraction of true ions, which is produced also within the spatial acceptance region of the TOF. The third factor τ_{axial} is the total axial transmission of the TOF meshes (cf. Sec. II A). Both factors are independent of the ion charge $n+$ and therefore do not contribute to the relative transmissions. The remaining factor, $\tau_{\text{dyn}} = \tau_{\text{dyn}}[m,T,t_{\text{extr}}(m,n+)]$ takes into account the fact that ions drift away from their initial positions due to their thermal energy. Assuming that the TOF entrance aperture is the radially limiting aperture, τ_{dyn} depends on the extraction time $t_{\text{extr}}(m,n+)$, which is the time from the creation of the ion until the moment when it reaches the TOF entrance aperture after acceleration by the extraction pulse. This extraction time is different for each ion species due to the charge- and mass-dependent axial acceleration of the ions. During the extraction process there is time for the ions to drift in the radial direction and leave or enter the acceptance area of the TOF.

In Fig. 3 the result of a model calculation is shown: in this calculation, the radial distribution of the initial positions of true ions was assumed to be Gaussian and symmetrical with respect to the TOF axis. A Maxwell-Boltzmann velocity distribution of ion velocities was assumed. The transmission factor τ_{dyn} was calculated as the fraction of ions that after extraction time t_{extr} were still located within the acceptance region of the TOF. The striped vertical bars in the lower part of Fig. 3 indicate typical extraction times for differently charged ions of the displayed elements. In the calculation, the distances and acceleration voltages described in Sec. II A were used, and for the radial distribution of ions a full half width of 1.5 mm was assumed. As one can see from Fig. 3, for Xe (300 K) the transmissions are nearly equal, while for La (2000 K) considerable differences are found for the different ion species due to the higher temperature.

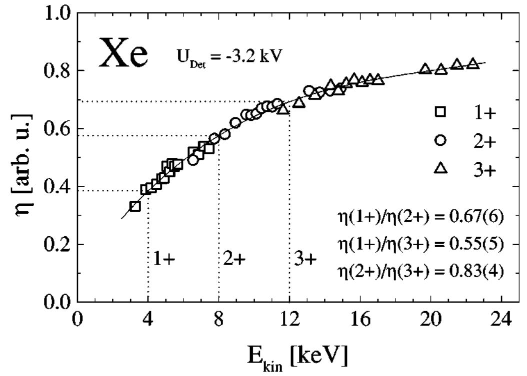

FIG. 4. Relative detection efficiency η of Xe ions, as a function of the kinetic energy E_{kin}, determined by variation of U_{acc}. U_{Det} denotes the detector voltage. A polynomial fit curve to the data is also shown (—). For a specific setting, $E_{\text{kin}} = -4$ kV, the relative efficiencies of $1+$, $2+$, and $3+$ ions are marked by dotted lines, and the resulting ratios $\eta(n+)/\eta(n'+)$ are displayed.

This model calculation, of course, only serves as an indicator of whether transmissions are relevant or not in the experiment. In the case of Xe there is no need to take transmissions into account for the given experimental configuration, while in the case of La relative transmissions are indeed relevant. However, they might be eliminated either by enlarging the TOF entrance aperture or by decreasing the extraction time t_{extr}.

Relative ion detection efficiencies

The detection efficiency η here denotes the fraction of ions that, upon hitting the detector, produce output pulses above the discriminator level that can be registered in the TDC stop input. Dead time effects of the detection system and the subsequent electronics, which may induce additional pulse losses, are not included in this definition.

As measurements from other authors show [12,13], for ions of the same mass but different charge states $n+$, to a good approximation η only depends on the kinetic energy E_{kin} of the ions hitting the detector; i.e., η is a unique curve of the kinetic energy, $\eta = \eta(E_{\text{kin}})$. In the present experiment, this kinetic energy is given by

$$E_{\text{kin}}(n+) = ne(U_{\text{extr}} + U_{\text{acc}}), \tag{10}$$

where U_{extr} is the voltage of the TOF extraction pulse and U_{acc} is the detector acceleration voltage (see Sec. II A).

This makes it possible to determine relative ion detection efficiencies $\eta(n+)/\eta(n_0+)$ by ‘‘standard’’ TOF measurements, where TOF cycles are triggered by a pulse generator (see Fig. 2). In a TOF measurement, the numbers of detector signals of the differently charged ion species are registered for a certain number of TOF cycles. By a series of measurements, varying U_{acc}, the number of detector signals is determined for each ion species as a function of E_{kin}. The result of an analysis of a channeltron detector is shown in Fig. 4. For three ion species, Xe 1+, 2+, 3+, the measured intensities are displayed on a relative scale. The intensities of the

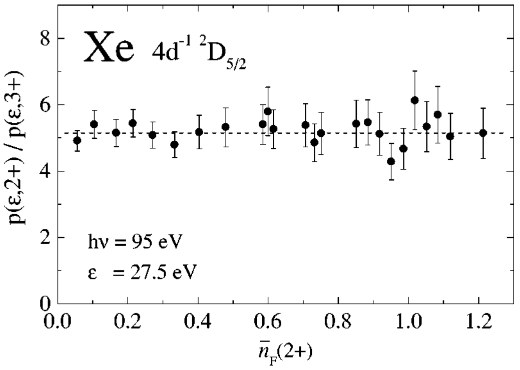

FIG. 5. Ratio of measured correlation probabilities $p(\epsilon,2+)$ and $p(\epsilon,3+)$ for Xe after decay of $4d_{5/2}^{-1}$ hole states as a function of source intensity. The source intensity is proportional to the average number of false coincidences per TOF cycle. In the figure the intensity scale is represented by $\overline{n}_F(2+)$. Dashed line: constant fit to data points.

different charge states have been rescaled by fixed factors to obtain a unique curve for $\eta(E_{\mathrm{kin}})$. For specific U_{extr} and U_{acc}, according to Eq. (10), relative detection efficiencies are extracted as indicated in the figure.

Numbers of true coincidences

The elimination of false coincidences from measured coincidence spectra and the determination of the average numbers of true coincidences $\overline{n}_T(n+)$ is a difficult problem, which was solved by the development of a sophisticated statistical evaluation procedure. This method is described in detail in Ref. [10]. Another approach for the determination of the coincidence rates was given by Kossmann [11]. Here, only a brief outline of the experimental aspects is given.

For each TOF coincidence spectrum, containing true and false coincidences, the distribution of false coincidences is determined by a reference measurement (''standard'' TOF measurement, see above). This distribution then has to be subtracted from the coincidence spectrum, taking into account specific dead time effects in signal registration. For the evaluation procedure it is important that both spectra are recorded under the same experimental conditions. This is achieved by switching every 5–10 s between electron trigger (coincidence mode) and random trigger (reference mode). Due to accumulation of false ions in the interaction region (see Ref. [10]), valid TOF starts must be separated by a minimum disable time. Both TOF spectra, registered in parallel, are then employed in calculating, channel by channel, the distribution of true coincidences. With the calculation procedure, a correction of signal losses due to dead time effects in the electronics is also performed. As an example, results of two measurements and reduced spectra of true coincidences are discussed in Sec. III.

The correct mode of operation of the evaluation procedure described in Ref. [10] has been tested by a series of coincidence-reference measurements of the Xe $4d_{5/2}^{-1}$ photoline for different source intensities (ionization rates). In these measurements, the source intensity and with it the rate of false coincidences was varied by a factor of about 20. As a result, in Fig. 5 the ratio of the correlation probabilities for the 2+ and 3+ charge state, $p(\epsilon,2+)/p(\epsilon,3+)$, evaluated from Eq. (7), is displayed as a function of the average number of false 2+ coincidences per TOF cycle, $\overline{n}_F(2+)$. The displayed ratio is constant within the experimental error bars, which demonstrates that false coincidences have been successfully eliminated in the evaluation.

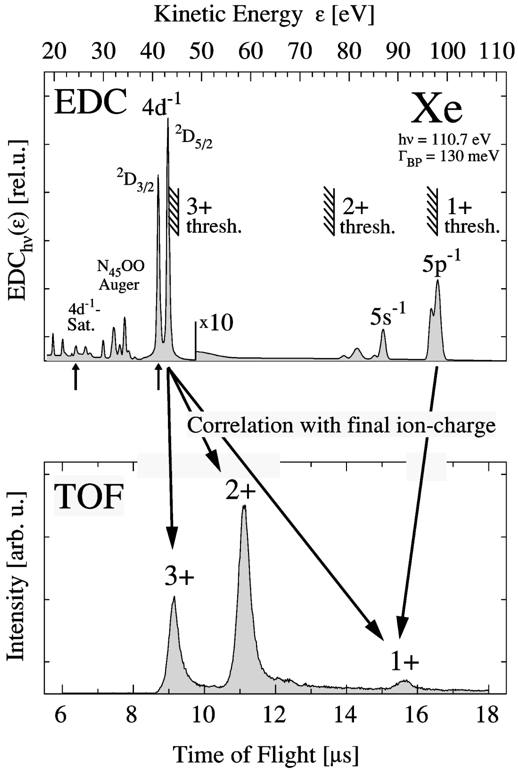

FIG. 6. Decay paths of excited singly ionized hole states of Xe into different final ion-charge states. Top: electron distribution curve [EDC(ϵ)] of Xe measured at a photon energy of 110.7 eV (thresholds from [17,24], short arrows indicate elctron energies ϵ of measured coincidence spectra of Fig. 8). Bottom: photoion time-of-flight (TOF) spectrum of Xe taken at the same photon energy.

III. FIRE SPECTROSCOPY: Xe IN THE REGION OF THE $4d\rightarrow\epsilon f$ RESONANCE

The prominent Xe $4d\rightarrow\epsilon f$ atomic shape resonance above threshold, which results from the repulsive centrifugal barrier in the effective potential for the excited ϵf electron, has stimulated many theoretical and experimental studies (see, for example, [14] and references therein). Apart from the partial cross sections and angular distribution asymmetry parameters for photoionization in the different subshells, the interest is focused on the decay of the $4d^{-1}$ hole states especially with respect to higher-order many-electron processes such as continuous (direct) double Auger decay with the simultaneous emission of two electrons. Such processes, giving rise to a continuous distribution in electron spectra, pose severe problems for a quantitative analysis. The pioneering work of Kämmerling *et al.* [7], showed that the electron-ion coincidence technique is able to determine directly decay probabilities of different decay routes. We have chosen the same example of the Xe $4d\rightarrow\epsilon f$ resonance to demonstrate the power of the coincidence method in its extended form of FIRE spectroscopy.

In its upper part, Fig. 6 shows a photoelectron spectrum

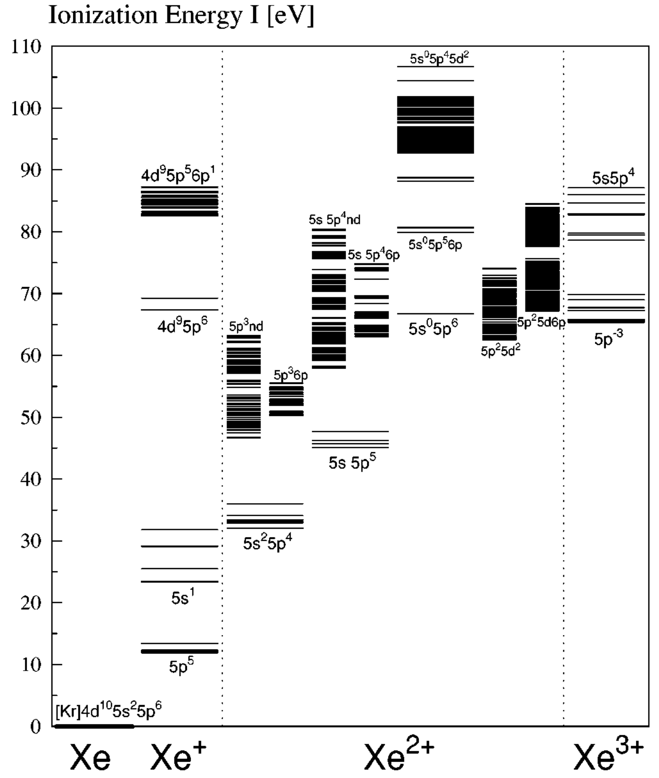

FIG. 7. Energy scheme obtained by (R)HF calculations using the Cowan code [17].

(EDC) taken at a photon energy of 110.7 eV, i.e., at the maximum of the broad $4d\rightarrow\epsilon f$ atomic shape resonance. One can see the main photolines due to photoionization in the $5p$, $5s$, and $4d$ subshells accompanied by corresponding satellite lines. At the left-hand side of the spectrum (low kinetic energy) one can also distinguish between several $N_{45}OO$ Auger lines due to the subsequent decay of $4d^{-1}$ states. In the lower part of Fig. 6, a photoion spectrum (TOF) of Xe taken at the same photon energy of 110.7 eV is depicted. The arrows between the photoelectron and the photoion spectrum indicate different decay routes for the creation of the final ion-charge states Xe^{n+} ($n=1$, 2, and 3). The $5s^{-1}$ or $5p^{-1}$ states of the main photolines, for example, are located energetically below the Xe^{2+} threshold (see also the energy scheme in Fig. 7) and therefore can be correlated only with Xe^{1+} ions.

The $4d^{-1}$ states are located above the Xe^{3+} threshold (but below the Xe^{4+} threshold) and can decay therefore into the three final charge states Xe^{1+}, Xe^{2+}, and Xe^{3+}. These final charge states are related to different possible decay routes: (A) decay of $4d^{-1}$ states to $5p^{-1}$ states by fluorescence leads to the formation of Xe^{1+}. (B) Auger decay of $4d^{-1}$ states to $5s^{-2}\epsilon\ell$, $5s^{-1}5p^{-1}\epsilon\ell$, and $5p^{-2}\epsilon\ell$ states leads to Xe^{2+}. From the occurrence of $N_{45}OO$ Auger lines in the electron spectrum one can deduce that those decay routes are rather probable. (C) Auger decay can be accompanied by the excitation of an additional electron. In the special case of continuum excitation of this electron, the process leads to the creation of Xe^{3+} (continuous double Auger decay). In the continuous double Auger decay, the energy is shared between the two simultaneously emitted electrons, thus giving rise to a continuous ''background'' in the electron spectrum. (D) Another possibility for the formation of Xe^{3+} is stepwise Auger decay of the $4d^{-1}$ hole states via Xe^{2+} states to Xe^{3+} states. In contrast to continuous double Auger [route (C)], here the two electrons have discrete kinetic energies giving rise to discrete Auger lines in the electron spectrum.

The $4d_j^{-1}$ hole states have certain probabilities $P(4d_j^{-1}\rightarrow n+)$ for the decay into different final charge states Xe^{n+} of the photoions. It is therefore a challenging task to determine these probabilities by the technique of photoelectron-photoion coincidence spectroscopy.

Figures 8(a) and 8(b) give two examples for such a photoelectron-photoion coincidence measurement at two specific electron energies, $\epsilon=41.2$ eV and $\epsilon=24.4$ eV. In the electron spectrum of Fig. 6, these energies correspond to the $4d_{3/2}^{-1}$ main line and one of the $4d^{-1}$ satellite lines

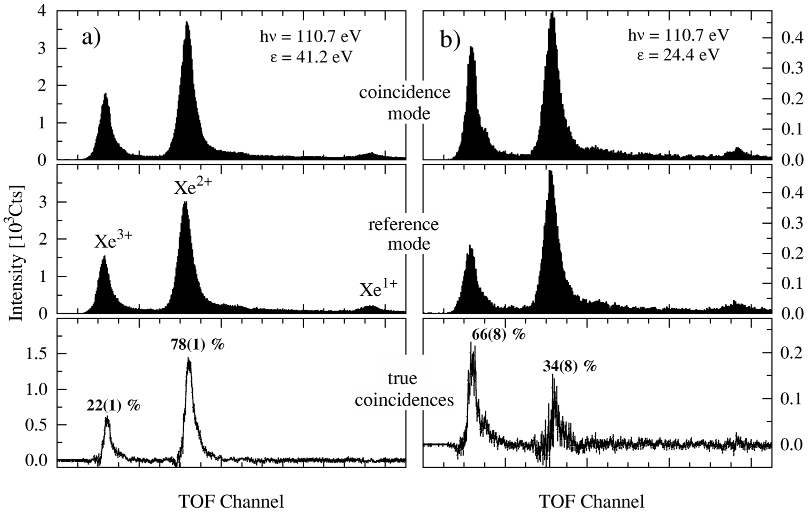

FIG. 8. Coincidence measurement (examples). Top: measured ion coincidence spectra of Xe taken at 110.7-eV photon energy, containing true and false coincidences; (a) kinetic electron energy $\epsilon=41.2$ eV corresponds to the $4d_{3/2}^{-1}$ photoline (data acquisition time 180 s); (b) kinetic electron energy $\epsilon=24.4$ eV corresponds to the $4d^{-1}$ satellite lines (data acquisition time 510 s). Middle: corresponding reference spectra of false coincidences. Bottom: spectra of true coincidences both calculated with a method described in Ref. [10].

[marked by short arrows (↑)], respectively. In the upper parts of Figs. 8(a) and 8(b), the measured distributions of Xe^{1+}, Xe^{2+}, and Xe^{3+} photoions in the coincidence mode are shown. These distributions include true and false coincidence signals. The middle parts give the corresponding distributions of the photoions obtained in the reference mode representing the distribution of false coincidences. As described in Sec. II B, the spectrum of true coincidences is deduced from coincidence spectrum and reference spectrum and is shown in the lower part of Figs. 8(a) and 8(b). For both initial ionic states one finds that the signal of Xe^{1+} vanishes, which means that the decay route (A) by fluorescence, yielding Xe^{1+}, can be neglected. With respect to the decay routes (B), (C), and (D) to Xe^{2+} and Xe^{3+} the results yield a remarkable difference for both ionic hole states. Whereas for the $4d_{3/2}^{-1}$ state [Fig. 8(a)] the dominant final ion-charge state is Xe^{2+}, the selected $4d^{-1}$ satellite state [Fig. 8(b)] preferably decays to Xe^{3+}. This means that for the $4d_{3/2}^{-1}$ state, the subsequent "normal" Auger decay of route (B) into Xe^{2+} is the main decay channel, while the shakeup state of the $4d^{-1}$ satellite has a very strong influence on the subsequent Auger decay favoring double Auger decay (continuous and stepwise) into Xe^{3+} [routes (C) and (D)].

For an accurate analysis of the decay probabilities of the $4d^{-1}$ states, one has to take into account that in the electron spectrum the corresponding photolines are partially superimposed on a background of direct double photoionization (shake-off) or continuous double Auger processes. That means that the start signals of the coincidence measurements for a definite electron energy ϵ, in this special case, are correlated with different processes. Therefore one has to distinguish between the measured correlation probabilities $p(\epsilon,n+)$ of the different final ion-charge states Xe^{n+} at a specific electron energy ϵ and the decay probability $P((nl_j)^{-1}\rightarrow n+)$ of a specific initial hole state.

In order to get information about the background caused by direct double photoionization or continuous double Auger, one has to perform coincidence measurements in the energy regions between the photolines. With the improved version of our experimental setup, we are now able to carry out coincidence measurements for a complete electron spectrum. In the present case, for example, approximately 100 coincidence spectra in the electron energy range $15\ \mathrm{eV}\leq\epsilon\leq 100\ \mathrm{eV}$ were obtained. The results of these measurements are shown in Fig. 9, where below the electron spectrum the measured correlation probabilities $p(\epsilon,1+)$, $p(\epsilon,2+)$, and $p(\epsilon,3+)$ are given. For a specific measurement at kinetic energy ϵ, the sum $\Sigma_{n=1}^{3}p(\epsilon,n+)$ is normalized to 1, according to Eq. (1).

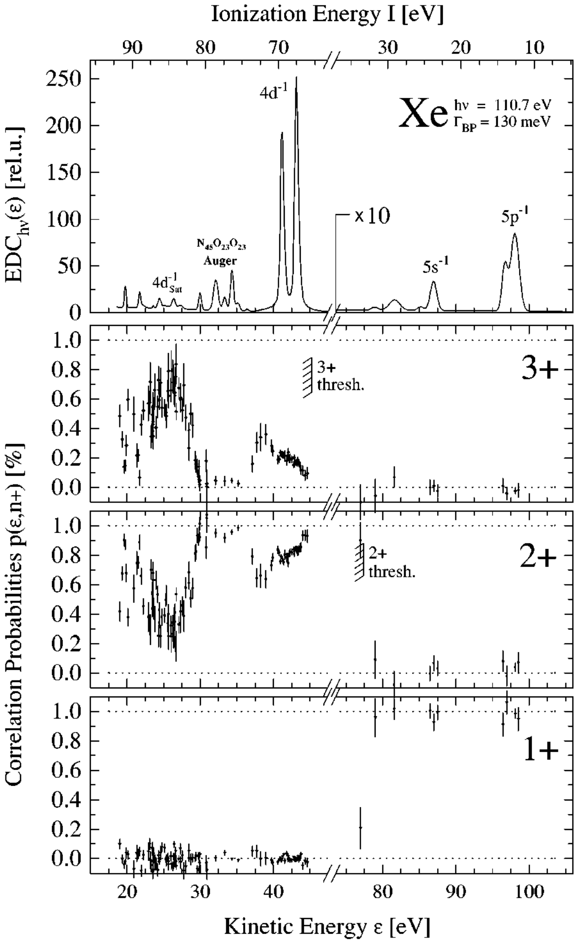

FIG. 9. Top: measured electron spectrum of Xe taken at 110.7-eV photon energy. Bottom: measured correlation probabilities between electrons of kinetic energy ϵ and different final ion-charge states Xe^{1+} to Xe^{3+}.

The correlation probability $p(\epsilon,1+)$ for the creation of singly charged (Xe^{1+}) photoions shows the expected behavior of $p\approx 1$ for $\epsilon>78$ eV (i.e., below the threshold of Xe^{2+}). For $\epsilon<45$ eV (i.e., in the region of the $4d$ ionization) the vanishing correlation probability $p(\epsilon,1+)$ indicates that fluorescence decay of $4d^{-1}$ states by processes like $4d^{-1}\rightarrow 5p^{-1}+h\nu$, in which the final ionic state is located below the Xe^{2+} threshold, can be neglected within the experimental error bars. Dramatic changes in the correlation probabilities $p(\epsilon,2+)$ and $p(\epsilon,3+)$ for doubly and triply charged photoions Xe^{2+} and Xe^{3+} occur in the region of the $4d$ ionization. These are caused by different processes like direct $4d$ photoionization (main lines), $4d$ photoionization with excitation (satellite lines), Auger decay (Auger lines), and direct double photoionization and continuous double Auger decay, which produce a continuous background in the electron spectrum.

For a discussion of these processes we introduce a more convenient representation of the results. By multiplying the electron spectrum $\mathrm{EDC}_{h\nu}(\epsilon)$ (or a fitting curve to it) with the correlation probabilities $p(\epsilon,n+)$ for fixed $n+$, one obtains the final ion-charge resolved electron (FIRE) spectrum:

$$\mathrm{EDC}_{h\nu}^{n+}(\epsilon)=p(\epsilon,n+)\mathrm{EDC}_{h\nu}(\epsilon). \tag{11}$$

$\mathrm{EDC}_{h\nu}^{n+}(\epsilon)$ represents the contribution to $\mathrm{EDC}_{h\nu}(\epsilon)$ of photoionization processes ending up in a $n+$ final ion-charge state. The sum of all these contributions results in the original electron spectrum:

$$\sum_{n+}\mathrm{EDC}_{h\nu}^{n+}(\epsilon) = \underbrace{\left(\sum_{n+}p(\epsilon,n+)\right)}_{=1}\ \mathrm{EDC}_{h\nu}(\epsilon) = \mathrm{EDC}_{h\nu}(\epsilon).$$

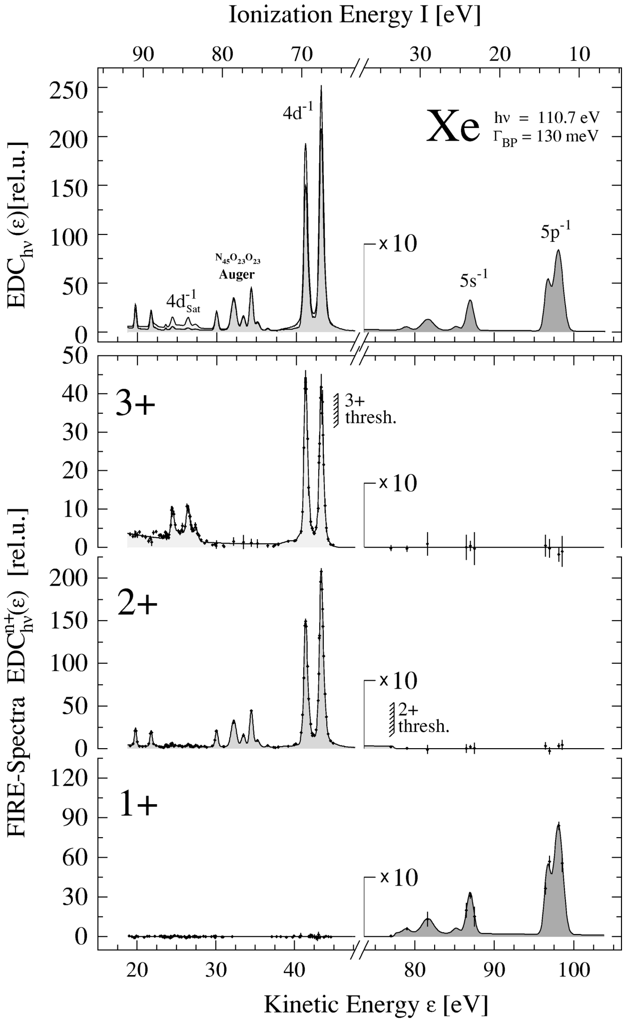

FIG. 10. Top: fitting curve to measured electron spectrum of Fig. 9. Different layers under the curve correspond to contributions of different FIRE spectra. Bottom: FIRE spectra for the charge states Xe^{1+} to Xe^{3+}.

Figure 10 shows the fitting curve to the measured electron spectrum of Fig. 9 (above) and its final ion-charge resolved contributions $\mathrm{EDC}_{h\nu}^{n+}(\epsilon)$, $n=1,2,3$ (below).

The region of high kinetic energy $\epsilon > 78$ eV (i.e., below the threshold of Xe^{2+}) shows a contribution of 100% by singly charged photoions Xe^{1+}, whereas the region of low kinetic energy $\epsilon < 45$ eV (i.e., above the threshold of Xe^{3+}) is characterized by the vanishing contribution of Xe^{1+} and the varying contributions of Xe^{2+} and Xe^{3+}. For a better demonstration of these variations we have plotted the FIRE spectra of Xe^{2+} and Xe^{3+} again for the different kinetic energy ranges ϵ of $4d^{-1}$ main lines and the $4d^{-1}$ satellite lines.

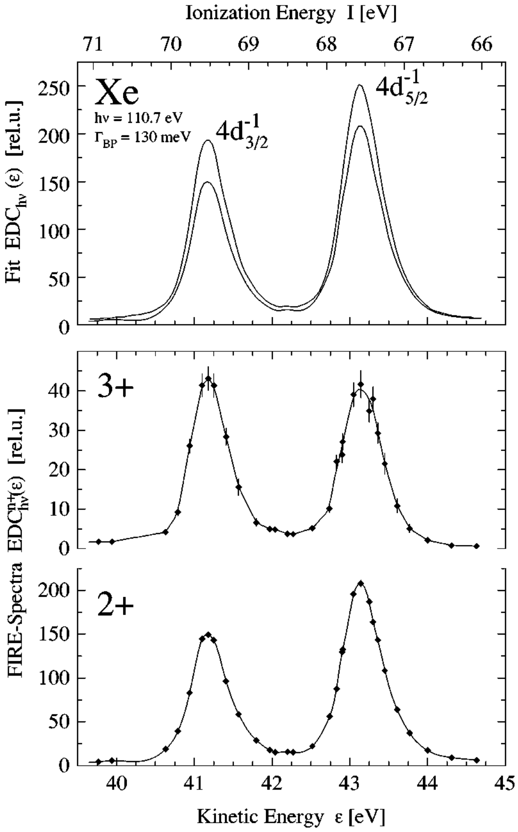

FIG. 11. Top: measured electron spectrum of Xe taken at 110.7-eV photon energy in the region of the $4d$ main lines. Bottom: FIRE spectra for the charge states Xe^{2+} and Xe^{3+}. Xe^{1+} final charge states were not observed within the error bars and have been omitted for clarity.

$4d^{-1}$ main lines

Figure 11 shows FIRE spectra at $h\nu = 110.7$ eV of the main photolines $4d^{-1}_{3/2}$ and $4d^{-1}_{5/2}$ at $\epsilon = 39-45$ eV. The decay probabilities $P(4d_j^{-1} \rightarrow n+)$ for the main photolines to Xe^{2+} and Xe^{3+} derived from the spectra in Fig. 11 are given in Table I. Comparison with the results of Kämmerling *et al.* [7] shows excellent agreement. Using the branching ratio of $4d^{-1}_{5/2}:4d^{-1}_{3/2} = 1.3:1$ [15], one gets a mean value for the double Auger decay of $P(4d^{-1} \rightarrow 3+) = 0.188(9)$ from our experimental data. With the combination of photoion and photoelectron data, Becker *et al.* [14] and Kämmerling *et al.* [16] estimated mean values of $P(4d^{-1} \rightarrow 3+) = 0.215$ and $P(4d^{-1} \rightarrow 3+) = 0.24$, respectively, which are slightly higher than our direct measured results. The $4d^{-1}$ states are located only 3–5 eV above the first Xe^{3+} threshold. The contribution to the double Auger decay is different for the fine structure components $4d^{-1}_{3/2}$ and $4d^{-1}_{5/2}$. The decay probability $P(4d^{-1}_{3/2} \rightarrow 3+) = 0.219(9)$ for the component with higher ionization energy is larger than the corresponding value $P(4d^{-1}_{5/2} \rightarrow 3+) = 0.165(9)$. This may be due to a

TABLE I. Decay probabilities $P(4d^{-1} \rightarrow n+)$ of the $4d^{-1}$ main lines to Xe^{2+} and Xe^{3+}.

	This work		Results of Ref. [7]		(R)HF calculations[b]	
	2+	3+	2+	3+	2+	3+
$4d^{-1}_{5/2}$	0.835(9)	0.165(9)	0.825(15)	0.175(15)	0.93	0.07
$4d^{-1}_{3/2}$	0.781(9)	0.219(9)	0.783(15)	0.217(15)	0.92	0.08
$4d^{-1}$	0.812(9)	0.188(9)	0.807(15)	0.193(15)	0.93	0.07

[a] Kaemmerling *et al.*

[b] Using the Cowan code, Ref. [17].

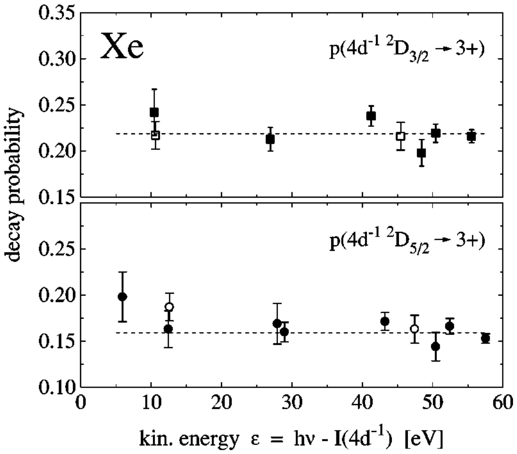

FIG. 12. Measured decay probabilities of the Xe $4d_{3/2}^{-1}$ and $4d_{5/2}^{-1}$ hole states into 3+ final charge states as a function of the kinetic energy ϵ of the emitted primary photoelectron. Filled symbols: this work. Open symbols: from Ref. [7]. Dashed line: weighted average of given data.

larger number of Xe^{3+} final states, which can be reached starting from the $4d_{3/2}^{-1}$ component.

The values in the last two columns of Table I are based on (R)HF calculations using the Cowan code [17]. For the Auger decay into Xe^{3+} it is assumed that all Xe^{2+} states above the Xe^{3+} threshold, which are populated by the first step of the $4d^{-1}$ decay into Xe^{2+}, will further decay into Xe^{3+}. Although the absolute difference between the calculated decay probability $P(4d_j^{-1} \rightarrow 3+)$ and the experimental value is only about 0.1, this corresponds to a relative difference of a factor of 2. This is the case even when a large number of basis configurations, shown in Fig. 7, is used.

Moreover, we investigated whether the kinetic energy of the $4d^{-1}$ photoelectrons influences the following decay processes, by measuring the decay probabilities of the $4d^{-1}$ hole states at different photon energies $h\nu$. Figure 12 shows the probabilities $P(4d_{5/2}^{-1} \rightarrow 3+)$ and $P(4d_{3/2}^{-1} \rightarrow 3+)$ for a series of measurements in the region of $\epsilon = I - h\nu = 6 - 58$ eV, demonstrating that above $\epsilon > 6$ eV the probabilities remain constant within the error bars. Only very close to threshold the decay probabilities might be influenced by postcollision interaction (PCI) (see Borst and Schmidt [18] and references therein) between photo and Auger electrons.

$4d^{-1}$ satellite lines

By a number of studies the decay of the descrete resonances Xe $4d^{-1}np$ has been investigated where a large double Auger yield was found [19,20]. In case of the $4d$ photoionization with additional excitation of a $5p$ electron to $4d^{-1}5p^{-1}6p$ states [21,22] the investigation is more complicated because of the overlap with the much stronger $4d$ photoionization (main process), resulting in an extended Auger structure. FIRE spectra of the $4d^{-1}$ satellite lines and $N_{45}OO$ Auger lines in the kinetic energy range $\epsilon = 23 - 31$ eV taken at a photon energy $h\nu = 110.7$ eV are depicted in Fig. 13. The 100% contribution of doubly charged photoions of the line at $\epsilon = 30$ eV is consistent with the assignment to $N_5O_{23}O_{23}\,{}^1S_0$ Auger decay. For the determination of the decay probabilities of the $4d^{-1}$ satellite states a contribution of background has to be taken into consideration. The inset in the upper part of Fig. 13 shows again the electron spectrum at $h\nu = 110.7$ eV in comparison with an electron spectrum taken at $h\nu = 104.7$ eV. In the latter spectrum at $h\nu = 104.7$ eV weak Auger lines can be seen in the region of the $4d^{-1}$ satellite lines ($\epsilon = 23 - 28$ eV) for $h\nu = 110.7$ eV. These Auger lines (corresponding to line No. 10-14, notation of Werme *et al.* [23]) are correlated with normal Auger decay ending up in a Xe^{2+} final ion-charge state and therefore have to be taken into account in the 2+ FIRE spectrum. The 3+ FIRE spectrum may contain an increasing continuous background for decreasing kinetic energy ϵ which could be due to double Auger decay of $4d^{-1}5p^{-1}np$ satellite states. The deduced decay probabilities for the strongest $4d^{-1}$ satellite states at $I = 86.4$ eV and $I = 84.4$ eV after these background corrections are shown in

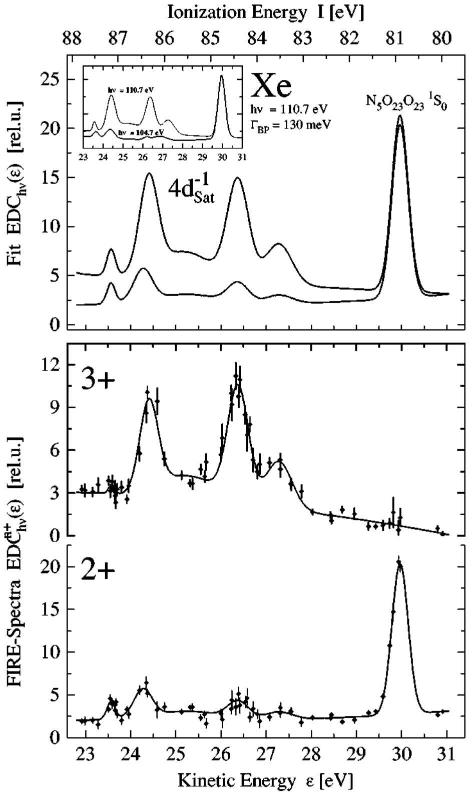

FIG. 13. Top: measured electron spectrum of Xe taken at 110.7-eV photon energy in the region of the $4d^{-1}$ satellite lines. Inset: additional electron spectrum taken at 104.7-eV photon energy. Bottom: FIRE spectra for the charge states Xe^{2+} and Xe^{3+}. Xe^{1+} final charge states were not observed within the error bars and have been omitted for clarity.

TABLE II. Decay probabilities $P(4d^{-1} \rightarrow n+)$ of $4d^{-1}5p^{-1}6p$ satellite lines to Xe^{2+} and Xe^{3+}.

	This work		(R)HF calculations[a]	
	2+	3+	2+	3+
$I = 84.4$ eV	0.26(8)	0.74(8)		
$I = 86.4$ eV	0.29(8)	0.71(8)		
$4d^{-1}$ Sat.	0.27(10)	0.73(10)	0.38	0.62

[a] Using the Cowan code, Ref. [17].

Table II. The obtained mean value of 0.73(10) for the relative Xe^{3+} contribution on the decay of the $4d^{-1}$ satellite states is much higher than the corresponding value for the $4d^{-1}$ main lines (0.188(9), Table I).

The same tendency was found already by Becker *et al.* [14] and Kämmerling *et al.* [16] who estimated values for double Auger decay for the $4d^{-1}$ satellite states averaging over all $4d^{-1}$ ''shake-up'' processes, combining photoelectron and photoion data. The estimated average values for the relative Xe^{3+} contribution of 0.58 (Becker *et al.* [14]) and (0.54) (Kämmerling *et al.* [16]) are slightly smaller than the measured mean value 0.73(10) of the $4d^{-1}5p^{-1}6p$ states. However, these estimated values are very sensitive to the relative Xe^{3+} contribution $P(4d^{-1}\rightarrow 3+)$ of the $4d^{-1}$ main process. If one uses the measured mean value $P(4d^{-1}\rightarrow 3+)=0.188(9)$ instead of the estimated value $P(4d^{-1}\rightarrow 3+)=0.24$ from Kämmerling *et al.* [16] the estimation for the Xe^{3+} contribution of the $4d^{-1}$ satellite states yields a value of 0.90.

Similar (R)HF calculations as performed for the $4d^{-1}$ main lines have been carried out for the $4d^{-1}$ satellite states (Table II). The calculated mean value of 0.62 for the relative Xe^{3+} contribution is in rather good agreement with the measured mean value of 0.73(10) although the absolute difference is about 0.1 as in the case of the $4d^{-1}$ main lines.

All these results show that the double Auger decay of the $4d^{-1}$ satellite lines to Xe^{3+} final ion-charge states is the dominant process in analogy to the double Auger decay of the discrete resonances $4d^{-1}np$ to Xe^{2+} final ion-charge states.

In summary, we described an electron-ion coincidence experiment with energy-analyzed electrons. With the development of a sophisticated statistical evaluation procedure for the distinction between true and false coincidences (Ref. [10]) high counting rates were achieved. We were able to split an electron spectrum into the different contributions of the final ion-charge states (FIRE spectroscopy). With the example of xenon in the region of the $4d\rightarrow\epsilon f$ resonance we have shown that this method is a valuable tool for the investigation of complex decay routes of core excited atomic states.

ACKNOWLEDGMENTS

The financial support from the Deutsche Forschungsgemeinschaft (Project No. Zi183111-1) is gratefully acknowledged. This work was carried out with partial support of the European Union under the HCM program. The authors thank the staff at BESSY for assistance.

[1] P. Lablanquie, J. H. D. Eland, I. Nenner, P. Morin, J. Delwiche, and M.-J. Hubin-Franskin, Phys. Rev. Lett. **58**, 992 (1987).

[2] T. Hayaishi, E. Murakami, A. Yagishita, F. Koike, Y. Morioka, and J. E. Hansen, J. Phys. B **21**, 3203 (1988).

[3] T. Hayaishi, A. Yagishita, E. Shigemasa, E. Murakami, and Y. Morioka, J. Phys. B **23**, 4431 (1990).

[4] R. I. Hall, K. Ellis, A. G. McConkey, G. Dawber, L. Avaldi, M. A. MacDonald, and G. C. King, J. Phys. B **25**, 377 (1992).

[5] R. I. Hall, A. G. McConkey, L. Avaldi, K. Ellis, M. A. MacDonald, G. Dawber, and G. C. King, J. Phys. B **25**, 1195 (1992).

[6] E. Shigemasa, T. Koizumi, Y. Itoh, T. Hayaishi, K. Okuno, A. Danjo, Y. Sato, and A. Yogishita, Rev. Sci. Instrum. **63**, 1505 (1992).

[7] B. Kämmerling, B. Krässig, and V. Schmidt, J. Phys. B **25**, 3621 (1992).

[8] S. Baier, G. Gottschalk, T. Kerkau, T. Luhmann, M. Martins, M. Richter, G. Snell, and P. Zimmermann, Phys. Rev. Lett. **72**, 2847 (1994).

[9] T. Luhmann, Ch. Gerth, M. Martins, M. Richter, and P. Zimmermann, Phys. Rev. Lett. **76**, 4320 (1996).

[10] T. Luhmann, Rev. Sci. Instrum. **68**, 2347 (1997).

[11] W. Wiley and I. McLaren, Rev. Sci. Instrum. **26**, 1150 (1955); H. Kossmann, Meas. Sci. Technol. **4**, 16 (1993).

[12] B. L. Schram, A. J. H. Boeroom, W. Kleine, and J. Kistemaker, Physica (Amsterdam) **32**, 749 (1966).

[13] J. Ravon, Nucl. Instrum. Methods Phys. Res. **211**, 7 (1983).

[14] U. Becker, D. Szostak, H. G. Kerkhoff, M. Kupsch, B. Langer, R. Wehlitz, A. Yagishita, and T. Hayaishi, Phys. Rev. A **39**, 3902 (1989).

[15] B. W. Yates, K. H. Tan, L. L. Coatsworth, and G. M. Bancroft, Phys. Rev. A **31**, 1529 (1985).

[16] B. Kämmerling, H. Kossmann, and V. Schmidt, J. Phys. B **22**, 841 (1989).

[17] R. D. Cowan, *The Theory of Atomic Structure and Spectra* (University of California Press, Berkeley, 1981).

[18] M. Borst and V. Schmidt, Phys. Rev. A **33**, 4456 (1986).

[19] U. Becker, D. Szostak, M. Kupsch, H. G. Kerkhoff, B. Langer, and R. Wehlitz, J. Phys. B **22**, 749 (1989).

[20] E. von Raven, M. Meyer, M. Pahler, and B. Sonntag, J. Electron Spectrosc. Relat. Phenom. **52**, 677 (1990).

[21] S. Svensson, B. Eriksson, N. Mårtensson, G. Wendin, and U. Gelius, J. Electron Spectrosc. Relat. Phenom. **47**, 327 (1988).

[22] D. W. Lindle, T. A. Ferrett, P. A. Heimann, and D. A. Shirley, Phys. Rev. A **37**, 3808 (1988).

[23] L. O. Werme, T. Bergmark, and K. Siegbahn, Phys. Scr. **6**, 141 (1972).

[24] C. E. Moore, *Atomic Energy Levels*, Natl. Bur. Stand. (U.S.) Circ. No. 467 (U.S. GPO, Washington, D.C., 1971), Vol. III.